

**Low-level atmospheric turbulence dataset in China
generated by combining radar wind profiler and
radiosonde observations**

Deli Meng^{a, b}, Jianping Guo^{a, d*}, Juan Chen^c, Xiaoran Guo^a, Ning Li^a, Yuping
Sun^a, Zhen Zhang^{a, c}, Na Tang^a, Hui Xu^a, Tianmeng Chen^a, Rongfang Yang^f,
Jiajia Hua^b

^aState Key Laboratory of Severe Weather Meteorological Science and
Technology, Chinese Academy of Meteorological Sciences, Beijing 100081, China

^bXiong'an Atmospheric Boundary Layer Key Laboratory of China
Meteorological Administration, Beijing 100085, China

^cAVIC Leihua Electronic Technology Research Institute, Wuxi 214063, China

^dGuizhou New Meteorological Technology Co., Ltd, Guiyang 550001, China

^eDepartment of Atmospheric and Oceanic Sciences & Institute of Atmospheric
Sciences, Fudan University, Shanghai 200438, China

^fHebei Meteorological Technology and Equipment Center, Shijiazhuang 050022,
China

**Correspondence to:* Dr/ Prof. Jianping Guo (Email: jpguocams@gmail.com)

Abstract

Low-level atmospheric turbulence plays a critical role in cloud dynamics and aviation safety. Nevertheless, ~~altitude~~-resolved turbulence profiles remain scarce, largely owing to observational challenges. By leveraging collocated radar wind profiler (RWP) and radiosonde observations from 29 stations across China during 2023, a ~~high vertical~~ resolution dataset of low-level turbulence-related parameters are generated based on spectral width method. This dataset includes squared Brunt–Vaisala frequency (N^2), turbulent dissipation rate (ε), vertical eddy diffusivity (K), inner scale (l_0), and buoyancy length scale (L_B), which are provided twice daily at 00 and 12 UTC with a vertical resolution of 120 m, covering altitudes from 0.12 km to 3.0 km above ground level (AGL). Spatial analysis reveals significant regional disparities in turbulence-related parameters across China, where ε , K and L_B are higher in northwest and north China compared to south China, while N^2 and l_0 display an inverse spatial pattern. This contrasting geographical distributions suggest distinct atmospheric instability across China. In terms of seasonality, turbulence-related variables showed maxima during spring and summer. Vertical profiles characteristics show distinct altitudinal dependencies, ε , L_B and K exhibit progressive attenuation with altitude, while N^2 and l_0 increase with ~~altitude~~. Statistical analysis indicates that ε and K follow log-normal distributions, whereas l_0 and L_B align with Gamma distributions. This dataset is publicly accessible <https://doi.org/10.5281/zenodo.14959025> (Meng and Guo, 2025), which provides crucial insights into the fine-scale structural evolution of low-level turbulence. The preliminary findings based on the dataset have great implications for improving our understanding of pre-storm environment and conducting scientific planning and guiding of low-level flight routes in the emerging low-altitude economy in China.

Deleted: height

Formatted: Not Highlight

Deleted: high-resolution

Deleted: height

Field Code Changed

Short Summary

This study provides a [high vertical resolution](#) dataset of low-level atmospheric turbulence across China, using radar and weather balloon observations. It reveals regional and seasonal variations in turbulence, with stronger activity in spring and summer. The dataset supports weather forecasting, aviation safety, and low-altitude flight planning, aiding China's growing low-altitude economy and accessible at <https://doi.org/10.5281/zenodo.14959025>.

Deleted: high-resolution

Field Code Changed

68

69 1 Introduction

70 The low-level atmosphere below 3.0 km altitude serves as a critical interface for
71 planetary boundary layer (PBL) and cloud interactions, and convective initiation
72 processes (Marquis et al., 2021; Nowak et al., 2021). This dynamic transition zone
73 facilitates exchange of water vapor, thermal energy, moment flux, and aerosol particles
74 between Earth’s surface and free atmosphere (Muñoz-Esparza et al., 2018; Brunke et
75 al., 2022). The turbulence-driven exchanges can be quantitatively characterized by key
76 physical parameters N^2 , ϵ , K , L_0 , L_B , and atmospheric refractive index structure
77 constant (Cn^2) (Fukao et al., 1994; Wilson, 2004). These parameters collectively
78 govern the energy cascade processes and momentum transfer mechanisms that
79 dominate PBL thermodynamics. Accurately understanding the spatiotemporal
80 evolution of low-level turbulence is crucial not only for improving predictive skill of
81 severe convective systems through refined parameterization schemes but also
82 implementing operational safeguards for low-altitude aviation safety.

83 Therefore, advances have been made in recent years in observational techniques
84 for characterizing low-level turbulence. Conventional in-situ platforms include weather
85 balloons (e.g., Clayson and Kantha, 2008; Guo et al., 2016; Kohma et al., 2019), rocket
86 (Namboodiri et al., 2011) and aircraft (Nicholls et al., 1984; Brunke et al., 2022;
87 Chechin et al., 2023). Concurrently, unmanned aerial vehicles (UAVs) have
88 demonstrated growing potential in capturing low-level turbulence features that
89 traditional aircraft and radiosonde networks cannot systematically resolve (Shelekhov
90 et al., 2021). Nevertheless, these approaches face inherent limitations, such as high
91 operational costs, discontinuous temporal sampling, and spatially constrained coverage
92 limited to point measurements or linear transects. Such restrictions fundamentally
93 impede the acquisition of vertically resolved turbulence profiles with sufficient
94 spatiotemporal continuity.

95 To address these observational gaps, ground-based lidars and radars have emerged

Deleted: :

Deleted: turbulent dissipation rate (

Deleted:)

Deleted: inner scale (

Deleted:)

Deleted: buoyancy length scale (

Deleted:), vertical eddy diffusivity (K),

Formatted: Not Highlight

Formatted: Not Highlight

Formatted: Not Highlight

Formatted: Not Highlight

Formatted: Not Highlight

Deleted: Kohma et al., 2019;

104 as pivotal solutions (Gage and Balsley, 1978). RWP and coherent Doppler wind lidar
 105 systems have demonstrated effectiveness in obtaining turbulence parameters with both
 106 high temporal resolution and operational continuity (Sato and Woodman,
 107 1982; Hocking, 1985; Fukao et al., 1994; Nastrom and Eaton, 1997; Luce et al., 2023a;
 108 Meng et al., 2024).

109 ε in conjunction with K , I_0 , and L_B derivable from ε (Fukao et al., 1994), serve
 110 as critical determinants in radar-derived quantification of atmospheric turbulence
 111 metrics. Three principal methodological frameworks have emerged for retrieving ε in
 112 low-level atmosphere from RWP observations, namely the power method (Hocking,
 113 1985; Hocking and Mu, 1997), variance method (Satheesan and Murthy, 2002), and
 114 Doppler spectral width method (Nastrom, 1997; Dehghan and Hocking, 2011). The
 115 power method utilizes backscattered signal intensity modulated by refractive index
 116 fluctuations (Weinstock, 1981a; Cohn, 1995). The variance method establishes a direct
 117 mathematical relationship between ε and the variance of vertical velocity (Satheesan
 118 and Murthy, 2002). Comprehensive reviews by Cohn (1995), Gage and Balsley (1978),
 119 and Wilson (2004) have thoroughly evaluated their underlying assumptions, advantages,
 120 and limitations. As highlighted by Satheesan and Murthy (2002), the power method
 121 necessitates thermodynamic profiles, the variance method demands accuracy in
 122 Doppler measurements, particularly challenged by contamination from non-turbulent
 123 motions in vertical beam observations, while the influence of ground clutter and the
 124 differences in the calculation of various spectral broadening terms are the main factors
 125 contributing to the large uncertainty in turbulence spectral width. Most widely adopted
 126 is the Doppler spectrum width technique, which isolates turbulence-induced spectral
 127 broadening through systematic removal of non-turbulent contributions (e.g., Cohn,
 128 1995; Nastrom and Eaton, 1997; Eaton and Nastrom, 1998; Jacoby-Kaoly et al., 2002;
 129 Dehghan and Hocking, 2011; Kohma et al., 2019; Jaiswal et al., 2020; Solanki et al.,
 130 2022; Chen et al., 2022a,b; Luce et al., 2023b). The non-turbulent spectral widths are
 131 mainly contributed by beam broadening, shear effects, and gravity wave perturbations,
 132 which can be estimated by the algorithms proposed by Hocking (1985), Nastrom (1997),

Deleted: Radar wind profiler (

Deleted:)

Deleted: Turbulence dissipation rate (

Deleted:)

Deleted: and K

Formatted: Not Highlight

Formatted: Not Highlight

Deleted: ,

and Dehghan and Hocking (2011), respectively. Recent work by Chen et al. (2022b) identifies a critical vertical wind shear (VWS) threshold of 0.006 s^{-1} , beyond which turbulence spectral width retrievals become increasingly susceptible to negative value artifacts, highlighting unresolved challenges under extreme shear conditions that frequently accompany severe convective systems.

Complementing radar-based methodologies, the radiosonde measurements have been long used to derive the profiles of N^2 and ε using the Thorpe analysis method (Thorpe, 1977). Originally designed to diagnose turbulent overturning in the troposphere and lower stratosphere, this method enables cross-validation with radar-derived turbulence metrics through coordinated multi-platform campaigns (Clayson and Kantha, 2008; Wilson et al., 2014; Li et al., 2016; Kohma et al., 2019; Jaiswal et al., 2020; Lv et al., 2021; Rajput et al., 2022; Ko et al., 2024). Nevertheless, Thorpe analysis method is not suitable for the turbulence retrieval in the low-level atmosphere below 3.0 km AGL.

Even though significant stride has been made in calculating temporally continuous profiles of ε , other turbulence-related parameters such as l_0 , L_B , and K in the low atmosphere remains insufficiently analyzed, particularly on a national scale, largely due to the lack of concurrent observations of high vertical resolution temperature, humidity and wind profiles. Fortunately, the RWP observational network has been built up and operated by China Meteorological Administration (CMA), and most of RWP stations are collocated with radiosonde stations. Furthermore, attempts were made to retrieve all the above-mentioned turbulence metrics by combining the measurements of RWP and radiosonde by Solanki et al. (2022). This motivates us to construct such low-level turbulence dataset in China, enabling a holistic view of the turbulence features throughout China. The paper is structured as follows. Section 2 details the data sources and methodology, including instrumentation specifications from the observational station and the retrieval method employed for turbulence-related parameters. Section 3 presents a multi-scale analysis of turbulence dynamics, encompassing vertical profile examinations and spatiotemporal variation patterns of

Deleted: (see

Deleted: ,

Deleted:)

Formatted: Not Highlight

Deleted: demonstrates

Deleted: s

Deleted: exceeding

Deleted: where

Formatted: Not Highlight

Deleted: high-resolution

Deleted: sites

Deleted: sites

low-level turbulence in China. Finally, summary and concluding remarks are given in Section 4.

2 Data and Methodology

2.1 RWP and radiosonde measurements

As of December 31, 2023, CMA operates a modern vertical meteorological observing network consisting of 120 L-band radiosonde and over 200 RWP stations. Through a rigorous station selection process, 29 optimally co-located observation stations were identified (Fig. 1) based on systematic evaluation of spatial representativeness and instrument performance metrics. These stations are equipped with an advanced RWP-radiosonde synergetic observation system specifically designed for retrieving low-level turbulence-related parameters. The network spans latitudes from 16.83°N to 49.22°N and longitudes from 75.98°E to 129.47°E, covering China's primary geomorphological regions, ranging from coastal plains (-0.4 m above mean sea level, AMSL) to high-mountain plateaus (4,326.8 m AMSL). Detailed station information is provided in Table 1.

The RWP system provides continuous wind profiling from 0.12 km to 5.0 km AGL, with a temporal resolution of 6 minutes and a vertical resolution of 120 m within the low-level atmosphere. The system incorporates advanced signal processing techniques, including ground clutter suppression algorithms and adaptive spectral filtering, to mitigate ground clutter interference and enhance real-time data fidelity (Solanki et al., 2022; Guo et al., 2023).

The L-band radiosonde system delivers high vertical resolution profiles with a temporal resolution of 1 second and a vertical resolution of 5–8 m. Routine observations are conducted twice daily at 00 UTC and 12 UTC. The radiosonde data undergo rigorous quality control and have been widely used in previous studies to examine spatiotemporal variations in turbulence and instability within the free atmosphere and PBL (Guo et al., 2016; Lv et al., 2021; Sun et al., 2025). Although horizontal

Deleted: This study

Deleted: above ground level (

Deleted:)

Deleted: high-resolution

Deleted: vertical

displacement occurs between launch stations and balloon trajectories, the spatial exclusivity of these trajectories ensures non-overlapping sampling domains among stations. This spatial segregation, combined with high-density vertical profiling, enables statistically independent measurements of turbulence-related parameters at each station (Ko et al., 2024).

Prior to turbulence retrieval through RWP-radiosonde synergetic analysis, precipitation events were excluded using ground-based 1-minute precipitation observations. Profiles from the RWP and radiosondes were synchronized to a 6-minute time resolution, and data collected 30 minutes before and after precipitation events were excluded to minimize residual moisture effects on radar refractivity and balloon trajectory perturbations (Wu et al., 2024). This rigorous quality assurance process yielded 16,942 validated non-precipitation profiles, enabling statistically robust characterization of turbulence regimes across China.

2.2 Algorithms for the estimation of turbulence-related parameters

Figure 2 presents the flowchart illustrating the main steps involved in estimating the following turbulence-related parameters, N^2 , ε , l_0 , L_B , and K_ρ respectively.

N^2 is usually used as a parameter which indicates stability of the stratification which has units of units s^{-2} , and can be estimated based on the pressure and temperature profiles from radiosonde measurement (Lilly et al., 1974):

$$N^2 = \frac{g}{\theta} \frac{\partial \theta}{\partial z} \quad (1)$$

where g (units: $m^2 s^{-1}$) is the gravitational acceleration, z (units: m) is the altitude AGL, and θ (units: K) is the potential temperature as follows:

$$\theta = T \left(\frac{1000}{P} \right)^{0.286} \quad (2)$$

where T (units: K) denotes temperature, P denotes pressure (units: hPa).

ε represents rate of energy cascading to smaller and smaller eddies until the energy is transformed into heat at the Kolmogorov scale (Fukao et al., 2014), which has units of units $m^2 s^{-3}$. ε can be estimated by the Doppler spectral width method (Nanstrom,

Deleted: sites

Deleted: squared Brunt–Vaisala frequency (

Deleted:)

Deleted: turbulence dissipation rate (

Deleted:)

Formatted: Not Highlight

Deleted: inner scale (

Formatted: Not Highlight

Deleted:)

Deleted: buoyancy length scale (

Formatted: Not Highlight

Deleted:)

Deleted: vertical eddy diffusivity (

Deleted:)

Deleted: N

Formatted: Not Highlight

Formatted: Not Highlight

Deleted: h

Formatted: Indent: First line: 1,5 ch

Deleted:

Formatted: Not Highlight

Formatted: Not Highlight

Deleted:

Formatted: Not Highlight

Formatted: Indent: First line: 1,5 ch

Formatted: Not Highlight

Formatted: Not Highlight

Formatted: Superscript

Formatted: Superscript

Formatted: Not Highlight

Deleted: is

1997). Turbulent spectral broadening (σ_{turb}^2 units: $m^2 s^{-2}$) is quantified by deducting non-turbulent broadening components (i.e., beam broadening, shear broadening, and transient effects) from the observed spectral width (σ_{obs}^2 units: $m^2 s^{-2}$) (Dehghan and Hocking, 2011). The equation is as follows:

$$\sigma_{obs}^2 \approx \sigma_{turb}^2 + \sigma_{beam+shear}^2 \quad (3)$$

Beam and shear broadening ($\sigma_{beam,shear}^2$ units: $m^2 s^{-2}$) is calculated using the following equations (Dehghan and Hocking, 2011):

$$\sigma_{beam,shear}^2 = \frac{\theta_{0.5}^2}{k} u^2 \cos \alpha - a_0 \frac{\theta_{0.5}}{k} \sin \alpha \left(u \frac{\partial u}{\partial z} \zeta \right) + b_0 \frac{2 \sin^2 \alpha}{8k} \left(\frac{\partial u}{\partial z} \zeta \right)^2 + c_0 \sin^2 \alpha \cos^2 \alpha |u \xi| + d_0 \sin^2 \alpha \cos^2 \alpha \xi^2 \quad (4)$$

where $k = 4 \ln 2$, $\zeta = 2R \theta_{0.5} \sin \alpha$, $\xi = \frac{\partial u}{\partial z} \frac{\Delta R}{\sqrt{12}}$, $a_0 = 0.945$, $b_0 = 1.500$, $c_0 = 0.030$, $d_0 = 0.825$ (Dehghan and Hocking, 2011). α is the beam zenith angle of the radar beam, $\theta_{0.5}$ is the radar half-power beam width, R is the radar radial sampling distance (units: m), ΔR is the radial distance resolution, Δz is the vertical resolution, u (units: $m s^{-1}$) is the horizontal wind speed at R_0 , and $\frac{\partial u}{\partial z}$ (units: s^{-1}) is the VWS at R_0 .

ε can be expressed as a function of turbulence-induced spectral broadening through the following relationship:

$$\varepsilon = \sigma_{turb}^3 \left(\frac{4\pi}{1.6} \right)^{3/2} J^{-3/2} \quad (5)$$

The term J ($m^{2/3}$) can be computed numerically with an estimate of the mean wind speed provided by RWP as follows:

$$J = 12 \Gamma \left(\frac{2}{3} \right) \int_0^{\frac{\pi}{2}} d\varphi \int_0^{\frac{\pi}{2}} \sin^3 \psi \left(b^2 \cos^2 \psi + a^2 \sin^2 \psi + \frac{L^2}{12} \sin^2 \psi \cos^2 \varphi \right)^{\frac{1}{3}} d\psi \quad (6)$$

where Γ is the gamma function, $a = \frac{R \theta_{0.5}}{4 \sqrt{\ln 2}}$ is the radius of the pulse volume, $b = \frac{\Delta z}{8 \sqrt{\ln 2}}$ is the half-length of the pulse, L is the product of the mean wind speed and dwell time of the RWP during the sampling time, which can be expressed as $u_t \Delta t$, and a , b , and L have units of meters. The double integration is taken between 0 and $\pi/2$ for both spherical coordinates ψ and φ (Solanki et al., 2022).

In the inertial subrange, l_0 (units: m) represents the scale for determining the transition region between the viscous and inertial subranges, and L_R (units: m)

- Deleted: σ_{turb}
- Formatted
- Deleted: σ_{obs}
- Formatted
- Formatted: Indent: First line: 1,5 ch
- Formatted: Not Highlight
- Formatted
- Formatted: Not Highlight
- Formatted: Not Highlight
- Deleted: φ
- Formatted: Not Highlight
- Deleted: φ
- Formatted: Not Highlight
- Deleted: φ
- Formatted: Indent: First line: 1,5 ch
- Deleted: $\varphi \dots \cos 2\alpha \varphi$
- Formatted: Not Highlight
- Deleted: $\varphi \dots \cos 2\alpha \varphi$
- Formatted: Not Highlight
- Formatted
- Deleted: φ
- Formatted: Not Highlight
- Formatted: Not Highlight
- Deleted: is
- Formatted: Not Highlight
- Formatted: Indent: First line: 1,5 ch
- Formatted: Superscript
- Deleted: is computed
- Formatted: Not Highlight
- Deleted: $b^2 \cos^2 \psi + a^2 \sin^2 \psi + L^2 \sin^2 \psi \cos^2 \varphi$
- Deleted: L and
- Formatted: Not Highlight
- Formatted: Not Highlight
- Formatted: Not Highlight
- Formatted: Not Highlight
- Formatted: Not Highlight
- Formatted: Not Highlight
- Formatted: Space After: 6 pt, Widow/Orphan control
- Formatted: Not Highlight
- Formatted: Not Highlight

328 represents the scale for determining the transition region between the inertial and
 329 buoyancy subranges (Weinstock, 1978; Hocking, 1985; Fukao et al., 2014). L_B and l_0
 330 can be computed as follows:

$$L_B = \frac{2\pi}{0.62} \left(\frac{\varepsilon}{N^3} \right)^{1/2} \quad (7)$$

$$l_0 = 7.4 \cdot (v^3 / \varepsilon)^{1/4} \quad (8)$$

331 where v (units: $\text{m}^2 \text{s}^{-1}$) is the kinematic viscosity, $v = 2 \cdot 10^{-5} / \rho$, and ρ represents
 332 atmospheric density which can be calculated based upon the pressure and temperature
 333 profiles measured by radiosonde (Eaton and Nastrom, 1998; Solanki et al., 2022).

334 K is the ratio of the kinematic heat flux to the mean potential temperature gradient
 335 (Weinstock, 1981b), which has units of units $\text{m}^2 \text{s}^{-1}$. K can be calculated from the
 336 following equation:

$$K = \gamma \varepsilon N^{-2} \quad (9)$$

337 where γ is the mixing efficiency, whose value is empirically determined varying
 338 between 0.2 and 1 (Fukao et al., 2014). $\gamma \approx Ri_f / (1 - Ri_f)$, where Ri_f is the flux
 339 Richardson number, an important parameter in turbulence that is indicative of the ratio
 340 of buoyancy production to shear production (Fukao et al., 2014). A value of 0.25
 341 corresponding to $Ri_f = 0.20$ is used in this study (Clayson and Kantha, 2008).

342 3 Results and discussion

343 3.1 Horizontal distribution of turbulence-related parameters

344 The climatological analysis of low-level turbulence regime below 3.0 km AGL
 345 across China at 00 UTC and 12 UTC in 2023 (Fig. 3) reveals distinct spatial patterns in
 346 turbulence-related parameters. Those turbulence-related parameters contain gradient
 347 Richardson number (Ri) (Guo et al., 2016), N^2 , ε , K , L_B , and l_0 . To examine the
 348 regional changes in above-mentioned turbulence parameters, we divided China into
 349 four subregions, north China (NC), northwest China (NWC), south China (SC) and
 350 southwest China (SWC), respectively (Fig. 3a).

351 N^2 displays pronounced regional heterogeneity across China, characterized by

Deleted: the scales l_0 and L_B are the inner and buoyancy length scale of turbulence, respectively

Formatted: Not Highlight

Formatted: Indent: First line: 2,5 ch

Formatted: Indent: First line: 2,33 ch

Formatted: Indent: First line: 0,5 ch

Formatted: Indent: First line: 1 ch

Formatted: Not Highlight

Formatted: Not Highlight

Deleted: .

Formatted: Not Highlight

Formatted: Indent: First line: 2 ch

Formatted: Not Highlight

Formatted: Not Highlight

Formatted: Not Highlight

Formatted: Not Highlight

Formatted: Not Highlight

Deleted: $\gamma = 0.25$ is the mixing efficiency

Formatted: Not Highlight

Deleted: squared Brunt Vaisalä frequency (

Formatted: Not Highlight

Deleted:)

Deleted: gradient Richardson number (Ri), turbulence

dissipation rate (

Deleted:)

Deleted: vertical eddy diffusivity (

Deleted:)

Deleted:)

Deleted:)

Deleted: buoyancy length scale (

Formatted: Not Highlight

Deleted:)

Deleted:)

Deleted:)

Deleted:)

Deleted:)

Deleted:)

Deleted:)

Deleted:)

Deleted:)

Deleted:)

Deleted:)

Deleted:)

Deleted:)

Deleted:)

Deleted:)

Deleted:)

Deleted:)

Deleted:)

Deleted:)

Deleted:)

enhanced static stability in SC and diminished stratification in NWC (Figs. 3a and 3b). This may be associated with the smaller Ri in NWC, indicating a more unstable atmospheric stratification (Figs. 3a-d). This instability may arise from intensified surface-atmosphere interactions driven by the unique environmental conditions over NWC, including elevated solar radiation flux due to reduced cloud cover, the predominance of bare soil and rock substrates with low albedo, and enhanced sensible heat flux from arid landscapes, as compared with those in SC (Xu et al., 2021). As can be seen from Figs. 3e and 3f, turbulence is stronger in NC and NWC compared to SC, by approximately 1 to 1.5 orders of magnitude, which may be related to stronger mechanical driven from VWS and thermally driven convective mixing from surface heating (Chen et al., 2022b). The K shows two-order amplification in NWC (Figs. 3g-h), governed by the synergistic enhancement of ε and N^2 through Equation 9. This contrasts with SC's suppressed turbulence regime, where higher vegetation density and moisture increase atmospheric stability (Guo et al., 2016; Xu et al., 2021).

For the two turbulence scales, L_B demonstrates inverse spatial patterns compared to l_0 (Figs. 3i-l). L_B shows larger values across NC, NWC, and SWC, contrasted by smaller values in SC. Equation 8 indicates that L_B is proportional to ε and inversely proportional to N^3 , suggesting that smaller N^2 along with larger ε contributes to a larger value of L_B . In contrast, l_0 demonstrates an opposite distribution compared to L_B (Figs. 3i and 3j). Since l_0 is proportional to ρ^3 and inversely proportional to ε , lower ρ leads to larger l_0 values in SWC. As previously indicated, compared with SC, the strong sensible heat flux in NWC contributes to a more pronounced low-level turbulence characterized by larger L_B and smaller l_0 values.

Further analysis reveals that the climatological mean values for N^2 are $10^{-3.76} \text{ s}^{-2}$ at 00 UTC and $10^{-3.88} \text{ s}^{-2}$ at 12 UTC, while the corresponding values for Ri are 3.72 and 3.03, indicating greater atmospheric instability at 12 UTC. Under a more unstable atmosphere, turbulence is stronger at 12 UTC, with climatological values of $10^{-3.37} \text{ m}^2 \text{ s}^{-3}$, $10^{0.72} \text{ m}^2 \text{ s}^{-1}$, 240.5 m for ε , K and L_B , respectively. The enhancement in turbulence metrics at 12 UTC versus 00 UTC baseline originates from the delayed local solar noon

Deleted: (Figs. 3a-3d)

Deleted: vertical eddy diffusivity

in NWC (UTC+6 zones) compared to SC (UTC+8 zones). This leads to stronger turbulence (as shown in Figs. 3f, h) and larger maximum scale of eddy in the inertial subrange (Fig. 3l) in the NWC. Notably, low-level turbulence in SWC at 12 UTC exceeds those values in SC by $\sim 25\%$ (Figs. 3f, h, l), attributable to stronger surface heating over the Tibetan Plateau foothills and Taklamakan Desert.

3.2 Vertical structure and probability distribution function (PDF) characteristics of turbulence-related parameters

Figures 4a-f show the profiles of N^2 , Ri , ε , l_0 , L_B , and K at 12UTC on 16 July 2023, at Mingfeng in NWC, respectively. It is evident that the vertical structure characteristics of N^2 and Ri are similar (Figs. 4a and 4b). Below 1.0 km AGL, N^2 is lower than $10^{-4.60} \text{ s}^{-2}$ (Fig. 4a), and Ri is lower than 0.5 (Fig. 4b) which suggesting static instability within low-level atmosphere. In the altitude range from 1.5 to 3.0 km AGL, Ri exceed 1, suggesting that an increase in static stability is a common feature. As shown in Figs. 4c-4e, ε , K , and L_B display consistent vertical structure below 3.0 km AGL, characterized by a pronounced decreasing trend with altitude. ε varies from $10^{-5.2}$ to $10^{-4.0} \text{ m}^2 \text{ s}^{-3}$ (Fig. 4c), while K ranges from $10^{-2.1}$ to $10^{0.5} \text{ m}^2 \text{ s}^{-1}$ (Fig. 4d) in the low-level atmosphere. L_B can reach up to about 600 m at 0.5 km but decreases to around 50 m at 3.0 km AGL (Fig. 4e). Conversely, l_0 increased with altitude, ranging from approximately 0.03 m at 0.5 km to about 0.06 m at 3.0 km AGL (Fig. 4f). Reduced stratification N^2 and Ri synergistically intensify turbulent mixing within the low-level atmosphere and result in larger eddies in the inertial subrange. Furthermore, the intensity of turbulent motions and L_B diminishes with altitude, while l_0 increases (Ghosh, 2003).

Figure 5 demonstrates the vertical stratification through stability parameters (N^2 , Ri), turbulence characteristics (ε , K), and turbulence scales (l_0 , L_B) within the low-level atmosphere in 2023 across China. Below 1.5 km AGL, the values of N^2 and Ri at 12 UTC are markedly lower than those at 00 UTC (Figs. 5a and 5b), reflecting enhanced atmospheric instability. $\log_{10}\varepsilon$ shows a nearly linear decrease with increasing altitude below 3.0 km (Fig. 5c), exhibiting gradients of $-10^{-3.70} \text{ m}^2 \text{ s}^{-3} \text{ km}^{-1}$ at 00 UTC and -10^{-

Deleted: lower

Deleted: gradient Richardson numbers

Deleted: $Ri < 0.5$,

Deleted: confirm

$3.68 \text{ m}^2 \text{ s}^{-3} \text{ km}^{-1}$ at 12 UTC. This indicates stronger turbulence at lower altitudes, with minimal differences in decay rates. Aligned with ε , K decreases with altitude at rates of $-10^{-0.14} \text{ m}^2 \text{ s}^{-1} \text{ km}^{-1}$ (00 UTC) and $-10^{0.33} \text{ m}^2 \text{ s}^{-1} \text{ km}^{-1}$ (12 UTC), further supporting reduced turbulent mixing at higher altitudes (Fig. 5d). Larger values of L_B is observed at lower altitude, while the values of l_0 are larger at higher altitude (Figs. 5e, f) (Ghosh, 2003; Rajput et al., 2022). L_B decreases sharply with altitude, showing steeper gradients at 12 UTC (-180.6 m km^{-1}) compared to 00 UTC (-69.6 m km^{-1}), consistent with stronger turbulence (Fig. 5e). This logarithmic decline suggests rapid attenuation of large turbulent eddies with altitude. In contrast, l_0 increases with altitude at rates of 0.0083 m km^{-1} (00 UTC) and 0.0069 m km^{-1} (12 UTC), reflecting a shift toward smaller-scale turbulence between the viscous and inertial subranges at higher altitudes (Fig. 5f). Marked vertical variability in L_B and l_0 dynamics reveal turbulence-stratification coupling mechanisms.

Figure 6 presents the PDFs for low-level atmospheric stability parameters (N^2 , Ri), turbulence metrics (ε , K), and turbulence scales (l_0 , L_B). It can be observed that $\text{Log}_{10} N^2$ exhibit an approximately Beta-like distribution, with standard deviations of $10^{-3.72} \text{ s}^{-2}$ at 00 UTC and $10^{-3.78} \text{ s}^{-2}$ at 12 UTC (Fig. 6a). Ri displays characteristics of an approximate Gamma distribution (Fig. 6b), consistent with its sensitivity to shear-driven instabilities. Both ε and K show traits typical of log-normal distributions (Rajput et al., 2022), with standard deviations of $10^{-3.11} \text{ m}^2 \text{ s}^{-3}$ ($10^{-3.07} \text{ m}^2 \text{ s}^{-3}$) for ε , and $10^{0.93} \text{ m}^2 \text{ s}^{-1}$ ($10^{1.09} \text{ m}^2 \text{ s}^{-1}$) for K at 00UTC (12UTC), respectively (Figs. 6c-d). For the horizontal turbulence scale sizes, l_0 and L_B exhibit approximate Gamma distributions (Figs. 6e and 6f). l_0 exhibits standard deviations of 0.013 m (0.012 m) at 00 UTC (12 UTC), respectively. L_B displays larger variability deviations of 219.8 m (264.1 m) at 00 UTC (12 UTC), respectively. The distinct PDF shapes reflect fundamental differences in the statistical behavior of stability, turbulence, and mixing parameters. The near log-normal distributions of ε and K suggest Gaussian-like randomness in turbulent processes, while the Gamma and Beta-like distributions of Ri and $\text{Log}_{10} N^2$ align with their dependency on threshold-governed instabilities.

Deleted: buoyancy length

Formatted: Not Highlight

Deleted: inner scale

Formatted: Not Highlight

Formatted: Not Highlight

Deleted: N^2

Deleted: N^2

Formatted: Not Highlight

Figure 7 demonstrates the relationships among turbulence-related parameters, with their quantitative correlation coefficients systematically presented at 00 UTC and 12 UTC, respectively. Notably, $\text{Log}_{10}N^2$ and Ri exhibit strong covariation, reflecting progressive stratification breakdown during atmospheric destabilization. The correlation coefficients for $\text{Log}_{10}\epsilon$ with $\text{Log}_{10}N^2$ at 00 UTC (Fig. 7a) and 12 UTC (Fig. 7b) are -0.19 and -0.13, while the coefficients with Ri are -0.22 and -0.12, respectively. These values suggest that turbulence tends to be stronger in unstable atmospheric regimes. $\text{Log}_{10}K$ demonstrates robust covariance with $\text{Log}_{10}\epsilon$ ($R > 0.80$), whereas inverse mechanistic linkages emerge stability indices ($\text{Log}_{10}N^2$ and Ri). L_B exhibits divergent relationships, showing positive correlations with turbulent metrics ($R > 0.65$ with $\text{Log}_{10}\epsilon$ and $\text{Log}_{10}K$), while displaying inverse correlations with stability indices ($R < -0.45$ with $\text{Log}_{10}N^2$ and Ri). The characteristic l_0 shows an inverse pattern to L_B , with negative correlations to $\text{Log}_{10}\epsilon$ ($R < -0.80$) and $\text{Log}_{10}K$ ($R < -0.60$), but positive correlations with $\text{Log}_{10}N^2$ and Ri . The interaction manifests as a marked negative correlation between L_B and l_0 , with statistical confirmation of their anticorrelation pattern. These systematic correlations collectively suggest that atmospheric stability of stratification in the buoyancy subrange fundamentally modulate turbulent cascades and energy transfer processes through their coordinated effects on both buoyancy-dominated and shear-driven turbulent structures (Lotfy et al., 2019; Rajput et al., 2022).

3.3 Seasonal variation of turbulence-related parameters with atmospheric stability

The previous subsection analyzed the spatial distribution and vertical structure of climatological turbulence-related parameters across China. This subsection focuses on the temporal turbulent variation in low-level atmosphere.

Figures. 8-9 systematically delineates interannual variability and seasonal cyclic patterns of N^2 , Ri , ϵ , l_0 , L_B , and K . N^2 is lower in spring and summer, but higher in autumn and winter, indicating greater atmospheric instability during warmer months (Figs. 8a and 8b, Fig. 9a). In summer, N^2 reaches its minimum below 1.2 km AGL, indicating a more unstable stratification. Both ϵ and K exhibit higher values in spring

Deleted:

Deleted:

Deleted:

Deleted:

Deleted: inner scale

Formatted: Not Highlight

Deleted:

Deleted:

and summer, and lower values in autumn and winter, with an approximate increase of one order of magnitude during warmer seasons (Chen et al., 2022a) (Figs. 8c-f, Figs. 9c-d). L_B follows a similar seasonal pattern to ε and K (Figs. 8i-j, Fig. 9f), further supporting the link between turbulence intensity and turbulence scales in the buoyancy subrange. In contrast, the annual evolution of l_0 (Figs. 8g and 8h, Fig. 9e) is inversely related to ε and K , with smaller values in spring and summer and larger values in autumn and winter (Figs. 8g, 8h). The vertical profiles of ε , K , and L_B consistently decrease with altitude across all seasons, highlighting the altitude-dependent characteristics of turbulent processes.

The seasonal evolutions of ε at 00 UTC and 12 UTC are broadly similar, though ε is consistently stronger at 12 UTC, likely due to lower values of N^2 and Ri (Figs. 8a-b). In summer at 12 UTC, ε exceeds $10^{-3.5} \text{ m}^2 \text{ s}^{-3}$ at an altitude of 1.8 km AGL, whereas in winter, this altitude is only reached at 0.6 km. This highlights the influence of seasonal turbulent dynamics on the development of the PBL. This suggests the existence of a maximum descent gradient region for ε and K at the PBL top (Meng et al., 2024). At 12 UTC, the l_0 values at 0.5 km are 0.012 m in summer and 0.013 m in winter, while at 1.2 km, those values are 0.021 m in summer and 0.024 m in winter, respectively (Fig. 8i). The values of L_B at 12 UTC are 910 m in summer and 550 m in winter at an altitude of 0.5 km, respectively (Fig. 8j). At 1.2 km, the values of L_B are 570 m in summer and 300 m in winter, respectively, which is approximately half of the values observed at 0.5 km. The seasonal variations in turbulence parameters underscore the critical role of atmospheric stability and PBL processes in modulating low-level turbulence intensity and mixing.

As previously discussed, the low-level atmosphere at 12 UTC exhibits greater instability compared to 00 UTC, resulting in stronger turbulence. However, it should be noted that 12 UTC corresponds to local standard time (LST) between 18 and 20, during which the PBL may exist in either a mixed or transitional state (Guo et al., 2016). To further investigate the relationship between turbulence structure and atmospheric stability at 12 UTC, this study adopted $Ri < 0.25$ as an indicator of atmospheric

Deleted:

Formatted: Not Highlight

Deleted: LST

532 instability (Chen et al., 2022a).

533 Figure 10 shows the vertical and seasonal distribution frequency of $Ri < 0.25$ at 00
534 UTC and 12 UTC. A distinct seasonal variation in the occurrence frequency is observed.
535 Analysis of the occurrence frequency climatology reveals pronounced seasonality in
536 low-level instability, with peak intensity occurring and maximum eddies ($L_B \approx 573.9$ m)
537 at 12 UTC in May during the spring-summer transition period dominated by enhanced
538 thermal convection and synoptic-scale frontal activity (Chen et al., 2022a). This
539 seasonal maximum coincides with weakened static stability and enhanced turbulence
540 (Fig. 8), facilitating vigorous vertical mixing through buoyancy-driven plumes.
541 Conversely, autumn-winter months exhibit suppressed turbulence and smaller L_B
542 (minimum $L_B \approx 272.6$ m in January), corresponding to increased atmospheric
543 stratification and reduced surface heat fluxes under frequent temperature inversion
544 regimes (Xu et al., 2021).

545 Furthermore, a significant discrepancy exists between the occurrence frequency of
546 $Ri < 0.25$ at 00 UTC and 12 UTC. For instance, in May, the vertical mean frequency of
547 $Ri < 0.25$ at 12 UTC is 23.6%, whereas at 00 UTC it registers only 14.9%. This disparity
548 indicates a more unstable atmosphere and stronger turbulence at 12 UTC (Figs. 6d and
549 8c-f). Vertically, the frequency exhibits a decreasing trend with altitude, suggesting that
550 the vertical structure of atmospheric instability contributes to the altitude-dependent
551 attenuation of turbulence intensity (Figs. 5c-d and 8c-f).

552 Figure 11 presents the vertical structural distribution of correlations among
553 turbulence-related parameters. $\log_{10}\epsilon$ show positive correlations with occurrence
554 frequency of $Ri < 0.25$ across altitudes (Fig. 11a), though $\log_{10}K$ exhibits stronger
555 correlations (not shown). This indicates that K responds more sensitively to unstable
556 atmospheric instability, particularly at 12 UTC where the correlation coefficient
557 exceeds 0.5 at 1.0–2.0 km AGL. As shown in Fig. 11b, l_0 demonstrates significant
558 negative correlations ($R < -0.90$) with $\log_{10}\epsilon$ vertically, suggesting that enhanced
559 turbulence under lower atmospheric instability corresponds to smaller l_0 between the
560 viscous and inertial subranges (Fig. 11b). Conversely, L_B show significant positive

Deleted:

Formatted: Not Highlight

Deleted: buoyancy length scale

Deleted:

Deleted: height

Deleted: vertical eddy diffusivity

Deleted: ~

correlations with $\log_{10}\varepsilon$, implying that stronger turbulence enlarges the maximum turbulent eddies between the inertial and buoyancy subranges (Fig. 11c). The correlation between l_0 and L_B is more pronounced at lower altitudes but remains relatively stable above 1.0 km. Hence, when the instability of the low-level atmosphere increases, the enhanced turbulence expands the range of the inertial subrange (Rajput et al., 2022).

4 Summary and concluding remarks

The estimation of turbulence-related parameters can help improving the accuracy of short-term local weather forecasts. Despite its importance, detailed research on the structure of low-level atmospheric turbulence has been hindered by a lack of comprehensive observational data. This study aims to address this gap by investigating the temporal and spatial evolution patterns of low-level turbulence in China.

Using observational data from 29 co-located RWP and radiosonde stations across China, this research employs the Doppler spectrum width method to estimate critical parameters of lower-level atmospheric turbulence. These parameters include the N^2 , ε , l_0 , L_B , and K . A comprehensive dataset of turbulence-related parameters was developed at the station scale for China in 2023, with a temporal resolution of 6-minute and a vertical resolution of 120 m below 3.0 km AGL.

Spatially, low-level turbulence demonstrates significant geographical variability. Compared to SC, N^2 and l_0 are lower in NWC and NC, while ε , L_B , and K are higher. This indicates stronger turbulence in the NWC and NC. It can be concluded that the predominance of bare land with low soil moisture in NWC and NC results in higher sensible heat flux, promoting greater heat transfer to the PBL, more unstable atmospheric stratification, and stronger turbulence compared to the forested, high soil moisture regions of SC.

As altitude increases, ε , L_B , and K exhibit a decreasing trend, while N^2 and l_0 increase. The PDF of ε and K conform a log-normal distribution, whereas l_0 and L_B approximately follow a Gamma distribution. Temporally, turbulence-related parameters

Deleted: both

Deleted: squared Brunt–Vaisala frequency (

Deleted:)

Deleted: turbulent dissipation rate (

Deleted:)

Formatted: Not Highlight

Deleted: inner scale (

Formatted: Not Highlight

Deleted:)

Deleted: buoyancy length scale (

Formatted: Not Highlight

Deleted:)

Deleted: vertical eddy diffusivity (

Deleted:)

Deleted: south China (

Deleted:)

Formatted: Not Highlight

Formatted: Not Highlight

Deleted: northwest China (

Deleted:)

Deleted: north China (

Deleted:)

display pronounced seasonal variations, with stronger turbulence observed in spring and summer and weaker turbulence in autumn and winter. Additionally, turbulence intensity at 12 UTC is notably stronger than at 00 UTC, primarily due to the unstable atmospheric stratification with a larger occurrence frequency of $Ri < 0.25$.

Although the dataset of low-level atmospheric turbulence-related parameters developed in this study encompasses typical regions across China, the limited station density and sparse radiosonde observations constrain the dataset's ability to provide high spatiotemporal resolution turbulence profiles for the entire country. In future work, additional data sources, such as coherent Doppler wind lidars and reanalysis datasets, will be integrated to construct a more refined, grid-scale turbulence dataset for China, enabling a more comprehensive understanding of atmospheric turbulence dynamics.

Author contributions

JG designed the research framework and conceptualized this study; DM and JG conducted the experiment and drafted the initial manuscript; XG, NL and NT helped the data collection and carried out the quality control. YS and ZZ prepared all distributed turbulence-related datasets. JC, HX, TC, JH and RY contributed to the revision of the manuscript. All authors contributed to writing and reviewing the paper.

Competing interests

The contact author has declared that there are no competing interests for all authors.

Financial support

This manuscript was jointly under the auspices of the National Natural Science Foundation of China under grants of 42325501, the Chinese Academy of Meteorological Sciences under grant 2024Z003 and the Department of Science and Technology of Guizhou province under grant KXJZ [2024] 033. the CMA Xiong'an Atmospheric Boundary Layer Key Laboratory under grant of 2023LABL-B06.

Data availability

The low-level turbulence-related dataset in China can be accessed at <https://doi.org/10.5281/zenodo.14959025> (Meng and Guo, 2025).

References

- Brunke, M. A., Cutler, L., Urzua, R. D., Corral, A. F., Crosbie, E., Hair, J., Hostetler, C., Kirschler, S., Larson, V., Li, X. Y., Ma, P. L., Minke, A., Moore, R., Robinson, C. E., Scarino, A. J., Schlosser, J., Shook, M., Sorooshian, A., Thornhill, K. L., Voigt, C., Wan, H., Wang, H. L., Winstead, E., Zeng, X. B., Zhang, S. X., and Ziemba, L. D.: Aircraft observations of turbulence in cloudy and cloud-free boundary layers over the western north Atlantic ocean from ACTIVATE and implications for the earth system model evaluation and development, *J. Geophys. Res.-Atmos.*, 127, 24, 10.1029/2022jd036480, 2022.
- Chechin, D. G., Lüpkes, C., Hartmann, J., Ehrlich, A., and Wendisch, M.: Turbulent structure of the Arctic boundary layer in early summer driven by stability, wind shear and cloud-top radiative cooling: ACLOUD airborne observations, *Atmos. Chem. Phys.*, 23, 4685-4707, 10.5194/acp-23-4685-2023, 2023.
- Chen, Z., Tian, Y. F., and Lue, D. R.: Turbulence parameters in the troposphere-lower stratosphere observed by Beijing MST radar, *Remote Sens.*, 14, 18, 10.3390/rs14040947, 2022a.
- [Chen, Z., Tian, Y. F., Wang, Y. A., Bi, Y. H., Wu, X., Huo, J., Pan, L. J., Wang, Y., and Lü, D. R.: Turbulence parameters measured by the Beijing mesosphere-stratosphere-troposphere radar in the troposphere and lower stratosphere with three models: comparison and analyses, *Atmos. Meas. Tech.*, 15, 4785-4800, 10.5194/amt-15-4785-2022, 2022b.](#)
- Clayson, C. A. and Kantha, L.: On turbulence and mixing in the free atmosphere inferred from high-resolution soundings, *J. Atmos. Ocean. Technol.*, 25, 833-852, 10.1175/2007jtecha992.1, 2008.
- Cohn, S. A.: Radar Measurements of Turbulent eddy dissipation rate in the troposphere a comparison of techniques, *J. Atmos. Ocean. Technol.*, 12, 85-95, 10.1175/1520-0426(1995)012<0085:Rmoted>2.0.Co;2, 1995.
- Dehghan, A. and Hocking, W. K.: Instrumental errors in spectral-width turbulence measurements by radars, *J. Atmos. Sol.-Terr. Phys.*, 73, 1052-1068, 10.1016/j.jastp.2010.11.011, 2011.
- Eaton, F. D. and Nastrom, G. D.: Preliminary estimates of the vertical profiles of inner

Field Code Changed

Formatted: Not Highlight

Deleted: Journal of Geophysical Research-Atmospheres

Formatted: Not Highlight

Deleted: Atmospheric Chemistry and Physics

Formatted: Not Highlight

Deleted: Remote Sensing

Formatted: Not Highlight

Deleted: Chen, Z., Tian, Y. F., and Lue, D. R.: Turbulence parameters in the troposphere-lower stratosphere observed by beijing mst radar, Remote Sensing, 14, 18, 10.3390/rs14040947, 2022b.

Formatted: Not Highlight

Deleted: Journal of Atmospheric and Oceanic Technology

Formatted: Not Highlight

Deleted: Journal of Atmospheric and Oceanic Technology

Formatted: Not Highlight

Deleted: Journal of Atmospheric and Solar-Terrestrial Physics...

and outer scales from White Sands Missile Range, New Mexico, VHF radar observations, *Radio Sci.*, 33, 895-903, 10.1029/98rs01254, 1998.

Fukao, S., Hamazu, K., and Doviak, R. J.: Radar for meteorological and atmospheric observations, Springer, 10.1007/978-4-431-54334-3, 2014.

Fukao, S., Yamanaka, M. D., Ao, N., Hocking, W. K., Sato, T., Yamamoto, M., Nakamura, T., Tsuda, T., and Kato, S.: Seasonal variability of vertical eddy diffusivity in the middle atmosphere 1. Three-year observations by the middle and upper atmosphere radar, *J. Geophys. Res.-Atmos.*, 99, 18973-18987, 10.1029/94jd00911, 1994.

Gage, K. S. and Balsley, B. B.: Doppler radar probing of the clear atmosphere, *Bull. Amer. Meteorol. Soc.*, 59, 1074-1093, 10.1175/1520-0477(1978)059<1074:Drpotc>2.0.Co;2, 1978.

Ghosh, A. K., Jain, A. R., and Sivakumar, V.: Simultaneous MST radar and radiosonde measurements at Gadanki (13.5°N, 79.2°E) 2. Determination of various atmospheric turbulence parameters, *Radio Sci.*, 38, 12, 10.1029/2000rs002528, 2003.

Guo, J. P., Miao, Y. C., Zhang, Y., Liu, H., Li, Z. Q., Zhang, W. C., He, J., Lou, M. Y., Yan, Y., Bian, L. G., and Zhai, P.: The climatology of planetary boundary layer height in China derived from radiosonde and reanalysis data, *Atmos. Chem. Phys.*, 16, 13309-13319, 10.5194/acp-16-13309-2016, 2016.

Hocking, W. K.: Measurement of turbulent energy dissipation rates in the middle atmosphere by radar techniques A review, *Radio Sci.*, 20, 1403-1422, 10.1029/RS020i006p01403, 1985.

Hocking, W. K. and Mu, P. K. L.: Upper and middle tropospheric kinetic energy dissipation rates from measurements of $\overline{C_p^2}$ - review of theories, in-situ investigations, and experimental studies using the Buckland Park atmospheric radar in Australia, *J. Atmos. Sol.-Terr. Phys.*, 59, 1779-1803, 10.1016/s1364-6826(97)00020-5, 1997.

Jacoby-Koaly, S., Campistron, B., Bernard, S., Bénech, B., Girard-Ardhuin, F., Dessens, J., Dupont, E., and Carissimo, B.: Turbulent dissipation rate in the boundary layer via UHF wind profiler Doppler spectral width measurements, *Bound.-Layer Meteor.*, 103, 361-389, 10.1023/a:1014985111855, 2002.

Jaiswal, A., Phanikumar, D. V., Bhattacharjee, S., and Naja, M.: Estimation of turbulence parameters using aries st radar and gps radiosonde measurements: first results from the central himalayan region, *Radio Sci.*, 55, 18, 10.1029/2019rs006979, 2020.

Ko, H. C., Chun, H. Y., Geller, M. A., and Ingleby, B.: Global distributions of atmospheric turbulence estimated using operational high vertical-resolution radiosonde data, *Bull. Amer. Meteorol. Soc.*, 105, E2551-E2566, 10.1175/bams-d-

Deleted: Journal of Geophysical Research-Atmospheres

Formatted: Not Highlight

Formatted: Not Highlight

Deleted: Bulletin of the American Meteorological Society

Deleted: -:

Deleted: :

Deleted: -: art. no. 1014

Formatted: Not Highlight

Deleted: Atmospheric Chemistry and Physics

Deleted: -

Deleted: (

Deleted:)

Formatted: Not Highlight

Deleted: Journal of Atmospheric and Solar-Terrestrial Physics...

Deleted: Bulletin of the American Meteorological Society

Formatted: Not Highlight

23-0193.1, 2024.

Kohma, M., Sato, K., Tomikawa, Y., Nishimura, K., and Sato, T.: Estimate of turbulent energy dissipation rate from the VHF radar and radiosonde observations in the Antarctic, [J. Geophys. Res.-Atmos.](#), 124, 2976-2993, 10.1029/2018jd029521, 2019.

Li, Q., Rapp, M., Schrön, A., Schneider, A., and Stober, G.: Derivation of turbulent energy dissipation rate with the Middle Atmosphere Alomar Radar System (MAARSY) and radiosondes at Andoya, Norway, *Ann. Geophys.*, 34, 1209-1229, 10.5194/angeo-34-1209-2016, 2016.

Lilly, D. K., Waco, D. E., and Adelfang, S. I.: Stratospheric mixing estimated from high-altitude turbulence measurements, *J. Appl. Meteorol.*, 13, 488-493, 10.1175/1520-0450(1974)013<0488:Smefha>2.0.Co;2, 1974.

Lotfy, E. R., Abbas, A. A., Zaki, S. A., and Harun, Z.: Characteristics of turbulent coherent structures in atmospheric flow under different shear-buoyancy conditions, *Bound.-Layer Meteor.*, 173, 115-141, 10.1007/s10546-019-00459-y, 2019.

Luce, H., Kantha, L., and Hashiguchi, H.: Statistical assessment of a Doppler radar model of TKE dissipation rate for low Richardson numbers, [Atmos. Meas. Tech.](#), 16, 5091-5101, 10.5194/amt-16-5091-2023, 2023a.

Luce, H., Kantha, L., Hashiguchi, H., Lawrence, D., Doddi, A., Mixa, T., and Yabuki, M.: Turbulence kinetic energy dissipation rate: assessment of radar models from comparisons between 1.3 GHz wind profiler radar (WPR) and DataHawk UAV measurements, [Atmos. Meas. Tech.](#), 16, 3561-3580, 10.5194/amt-16-3561-2023, 2023b.

Lv, Y. M., Guo, J. P., Li, J., Cao, L. J., Chen, T. M., Wang, D., Chen, D. D., Han, Y., Guo, X. R., Xu, H., Liu, L., Solanki, R., and Huang, G.: Spatiotemporal characteristics of atmospheric turbulence over China estimated using operational high-resolution soundings, [Environ. Res. Lett.](#), 16, 13, 10.1088/1748-9326/abf461, 2021.

Muñoz-Esparza, D., Sharman, R. D., and Lundquist, J. K.: Turbulence dissipation rate in the atmospheric boundary layer: observations and WRF mesoscale modeling during the XPiA field campaign, [Mon. Weather Rev.](#), 146, 351-371, 10.1175/mwr-d-17-0186.1, 2018.

Marquis, J. N., Varble, A. C., Robinson, P., Nelson, T. C., and Friedrich, K.: Low-level mesoscale and cloud-scale interactions promoting deep convection initiation, [Mon. Weather Rev.](#), 149, 2473-2495, 10.1175/mwr-d-20-0391.1, 2021.

Namboodiri, K. V. S., Dileep, P. K., Mammen, K., Ramkumar, G., Kumar, N., Sreenivasan, S., Kumar, B. S., and Manchanda, R. K.: Effects of annular solar eclipse of 15 January 2010 on meteorological parameters in the 0 to 65 km region over Thumba, India, *Meteorol. Z.*, 20, 635-647, 10.1127/0941-2948/2011/0253, 2011.

Deleted: Journal of Geophysical Research-Atmospheres

Formatted: Not Highlight

Deleted: Atmospheric Measurement Techniques

Formatted: Not Highlight

Formatted: Not Highlight

Deleted: Atmospheric Measurement Techniques

Deleted: Environmental Research Letters

Formatted: Not Highlight

Formatted: Not Highlight

Deleted: Monthly Weather Review

Formatted: Not Highlight

Deleted: Monthly Weather Review

776 Nicholls, S.: The dynamics of stratocumulus Aircraft observations and comparisons
 777 with a mixed layer model, [Q. J. R. Meteorol. Soc.](#), 110, 783-820,
 778 10.1002/qj.49711046603, 1984.

779 Nowak, J. L., Siebert, H., Szodry, K. E., and Malinowski, S. P.: Coupled and decoupled
 780 stratocumulus-topped boundary layers: turbulence properties, [Atmos. Chem. Phys.](#),
 781 21, 10965-10991, 10.5194/acp-21-10965-2021, 2021.

782 Meng, D., Guo, J.: A low-level turbulence-related parameters dataset derived from the
 783 radar wind profiler and radiosonde in China during 2023. [Data
 784 set]. <https://doi.org/10.5281/zenodo.14959025>, 2025.

785 Meng, D. L., Guo, J. P., Guo, X. R., Wang, Y. J., Li, N., Sun, Y. P., Zhang, Z., Tang, N.,
 786 Li, H. R., Zhang, F., Tong, B., Xu, H., and Chen, T. M.: Elucidating the boundary
 787 layer turbulence dissipation rate using high-resolution measurements from a radar
 788 wind profiler network over the Tibetan Plateau, [Atmos. Chem. Phys.](#), 24, 8703-8720,
 789 10.5194/acp-24-8703-2024, 2024.

790 Nastrom, G. D.: Doppler radar spectral width broadening due to beamwidth and wind
 791 shear, *Ann. Geophys.-Atmos. Hydrospheres Space Sci.*, 15, 786-796,
 792 10.1007/s00585-997-0786-7, 1997.

793 Nastrom, G. D. and Eaton, F. D.: A brief climatology of eddy diffusivities over White
 794 Sands Missile Range, New Mexico, *Journal of Geophysical Research-Atmospheres*,
 795 102, 29819-29826, 10.1029/97jd02208, 1997.

796 Rajput, A., Singh, N., Singh, J., and Rastogi, S.: Investigation of atmospheric
 797 turbulence and scale lengths using radiosonde measurements of GVAX-campaign
 798 over central Himalayan region, [J. Atmos. Sol.-Terr. Phys.](#), 235, 16,
 799 10.1016/j.jastp.2022.105895, 2022.

800 Satheesan, K. and Murthy, B. V. K.: Turbulence parameters in the tropical troposphere
 801 and lower stratosphere, *Journal of Geophysical Research-Atmospheres*, 107, 13,
 802 10.1029/2000jd000146, 2002.

803 Sato, T. and Woodman, R. F.: Fine altitude resolution observations of stratospheric
 804 turbulent layers by the Arecibo 430-MHz radar, [J. Atmos. Sci.](#), 39, 2546-2552,
 805 10.1175/1520-0469(1982)039<2546:Faroos>2.0.Co;2, 1982.

806 Shelekhov, A. P., Afanasiev, A. L., Shelekhova, E. A., Kobzev, A. A., Tel'minov, A. E.,
 807 Molchunov, A. N., and Poplevina, O. N.: Using small unmanned aerial vehicles for
 808 turbulence measurements in the atmosphere, *Izv. Atmos. Ocean. Phys.*, 57, 533-545,
 809 10.1134/s0001433821050133, 2021.

810 Solanki, R., Guo, J. P., Lv, Y. M., Zhang, J., Wu, J. Y., Tong, B., and Li, J.: Elucidating
 811 the atmospheric boundary layer turbulence by combining UHF radar wind profiler
 812 and radiosonde measurements over urban area of Beijing, *Urban CLim.*, 43, 13,
 813 10.1016/j.uclim.2022.101151, 2022.

Formatted: Not Highlight

Deleted: Quarterly Journal of the Royal Meteorological Society...

Deleted: Atmospheric Chemistry and Physics

Formatted: Not Highlight

Formatted: Not Highlight

Deleted: Atmospheric Chemistry and Physics

Deleted: Journal of Atmospheric and Solar-Terrestrial Physics...

Formatted: Not Highlight

Formatted: Not Highlight

Deleted: Journal of the Atmospheric Sciences

821 Sun, Y., Guo J., Chen T., Li N., Guo X., Xu H., Zhang Z., Shi Y., Zeng L., Chen J.,
822 Meng D.: Long-term high-resolution radiosonde measurements reveal more
823 intensified and frequent turbulence at cruising altitude in China, *Geophys. Res. Lett.*,
824 52, e2024GL114076, /10.1029/2024GL114076, 2025.

825 Thorpe, S. A.: Turbulence and mixing in a Scottish Loch, *Philos. Trans. R. Soc. A-Math.*
826 *Phys. Eng. Sci.*, 286, 125-181, 10.1098/rsta.1977.0112, 1977.

827 Weinstock, J.: Vertical turbulent diffusion in a stably stratified fluid, *J. Atmos. Sci.*, 35,
828 1022-1027, 10.1175/1520-0469(1978)035<1022:Vtdias>2.0.Co;2, 1978.

829 Weinstock, J.: Using radar to estimate dissipation rates in thin layers of turbulence,
830 *Radio Sci.*, 16, 1401-1406, 10.1029/RS016i006p01401, 1981a.

831 Weinstock, J.: Vertical turbulence diffusivity for weak or strong stable stratification, *J.*
832 *Geophys. Res.-Oceans*, 86, 9925-9928, 10.1029/JC086iC10p09925, 1981b.

833 Wilson, R.: Turbulent diffusivity in the free atmosphere inferred from MST radar
834 measurements: a review, *Ann. Geophys.*, 22, 3869-3887, 10.5194/angeo-22-3869-
835 2004, 2004.

836 Wilson, R., Luce, H., Hashiguchi, H., Nishi, N., and Yabuki, Y.: Energetics of persistent
837 turbulent layers underneath mid-level clouds estimated from concurrent radar and
838 radiosonde data, *J. Atmos. Sol.-Terr. Phys.*, 118, 78-89, 10.1016/j.jastp.2014.01.005,
839 2014.

840 Wu, J. Y., Guo, J. P., Yun, Y. X., Yang, R. F., Guo, X. R., Meng, D. L., Sun, Y. P., Zhang,
841 Z., Xu, H., and Chen, T. M.: Can ERA5 reanalysis data characterize the pre-storm
842 environment? *Atmos. Res.*, 297, 18, 10.1016/j.atmosres.2023.107108, 2024.

843 Xu, Z. Q., Chen, H. S., Guo, J. P., and Zhang, W. C.: Contrasting effect of soil moisture
844 on the daytime boundary layer under different thermodynamic conditions in summer
845 over China, *Geophysical Research Letters*, 48, 11, 10.1029/2020gl090989, 2021.

Deleted: Journal of the Atmospheric Sciences

Formatted: Not Highlight

Formatted: Not Highlight

Deleted: Journal of Geophysical Research-Oceans

Formatted: Not Highlight

Deleted: Journal of Atmospheric and Solar-Terrestrial
Physics...

Deleted: Atmospheric Research

Formatted: Not Highlight

Table 1. Summary of the radar wind profiler (RWP) stations used in the calculation of turbulence related parameters.

ID	Station	Lon. (°E)	Lat. (°N)	Elevation (m)
50953	Harbin	126.58	45.93	115.0
51463	Urumqi	87.74	43.81	935.0
51839	Minfeng	82.69	37.07	1408.9
52533	Jiuquan	98.49	39.77	1477.2
53463	Hohhot	111.57	40.86	1152.1
53772	Taiyuan	112.58	37.62	785.0
53845	Yan'an	109.45	36.58	1180.4
54304	Zhangjiakou	115.27	40.95	726.0
54511	Beijing	116.47	39.81	31.5
54727	Zhangqiu	117.52	36.65	251.9
55664	Tingri	87.12	28.65	4326.8
56029	Yushu	96.96	33.00	3684.0
56146	Ganzi	100.00	31.62	3353.0
56173	Hongyuan	102.55	32.79	3465.0
56312	Linzhi	94.36	29.65	2988.4
56651	Lijiang	100.22	26.85	2382.4
56964	Simao	100.99	22.82	1423.3
57461	Sanxia	111.36	30.74	253.8
57516	Chongqing	106.46	29.58	260.0
57687	Changsha	112.79	28.11	46.0
57816	Guiyang	106.73	26.59	1223.7
58238	Nanjing	118.90	31.93	40.6
58459	Hangzhou	120.29	30.18	43.0
58633	Quzhou	118.89	28.99	86.4
58725	Shaowu	117.50	27.31	363.6
58847	Fuzhou	119.29	26.08	112.1
59312	Chaozhou	116.69	23.67	7.0
59431	Nanning	108.55	22.78	104.9
59758	Haikou	110.25	19.99	69.0

Figures

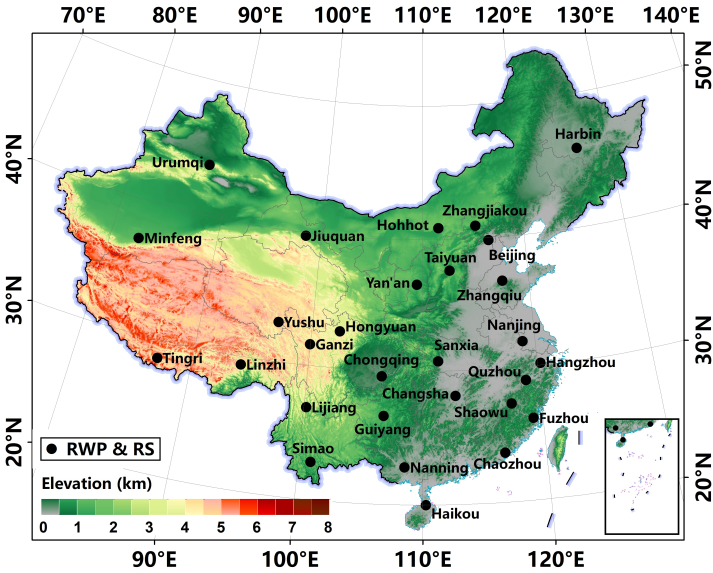
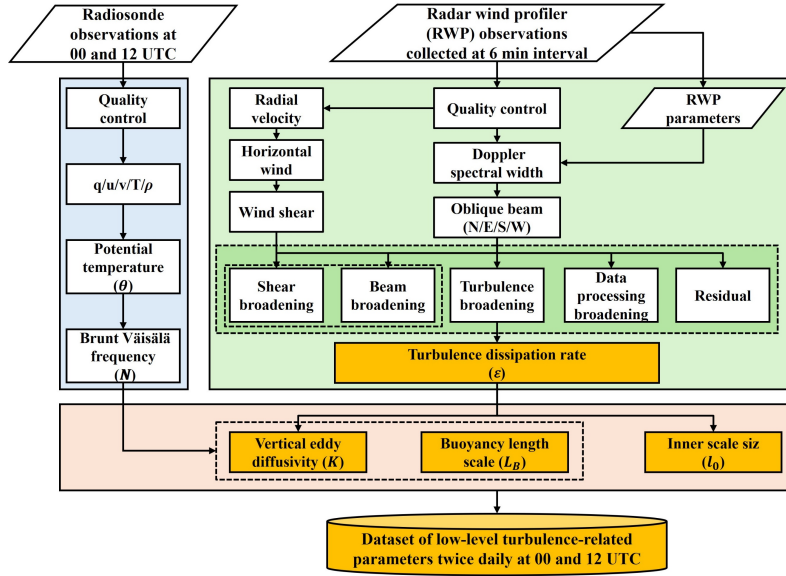


Figure 1. Spatial distribution of the co-located radar wind profiler (RWP) and radiosonde stations in China.



860

861 **Figure 2.** Flowchart used to generate the low-level atmospheric turbulence-related
 862 dataset at 00 UTC and 12 UTC in China. Turbulence-related parameters include squared
 863 Brunt Väisälä frequency (N^2), turbulent dissipation rate (ϵ), inner scale (l_0), buoyancy
 864 length scale (L_B), vertical eddy diffusivity (K), respectively.

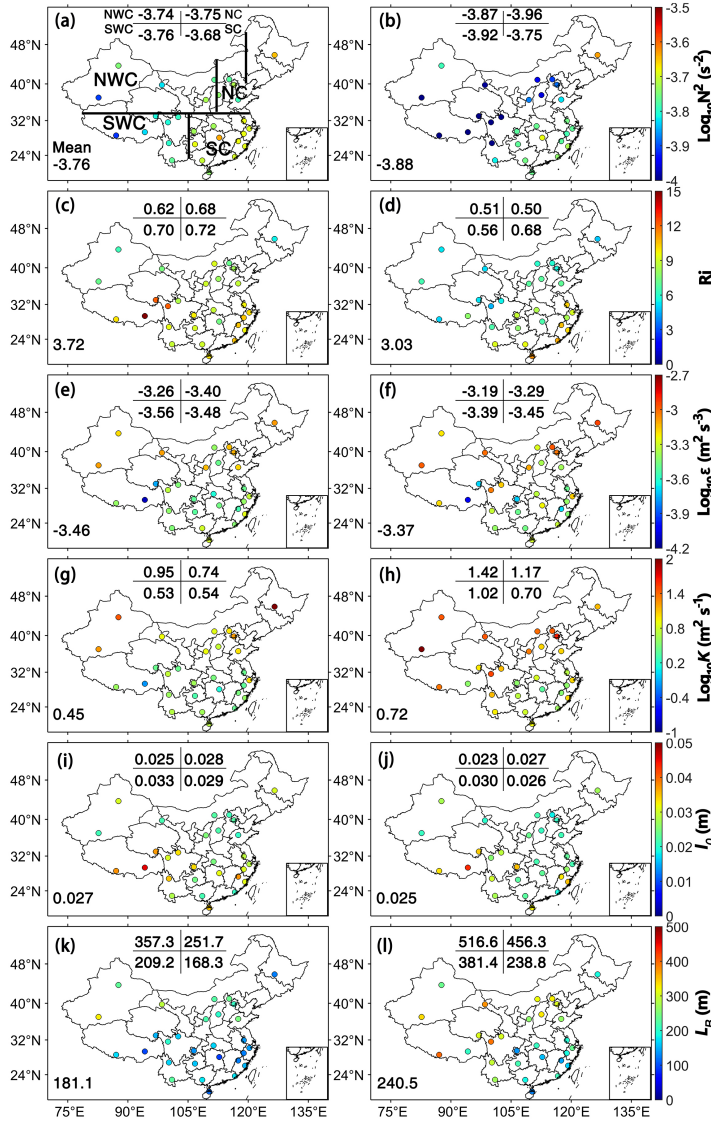
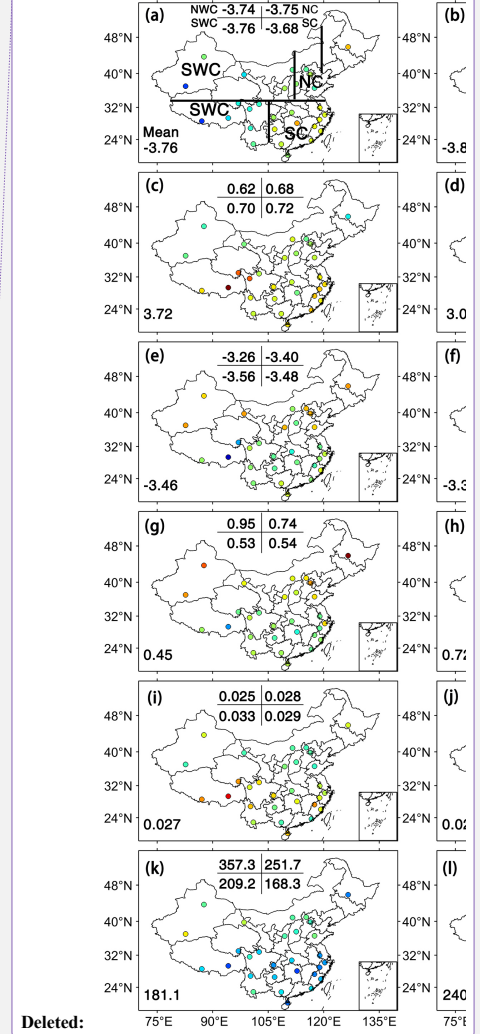


Figure 3. Spatial distribution and mean values of N^2 below 3.0 km above ground level (AGL) for 2023 at (a) 00 UTC and (b) 12 UTC, (c, d) Ri , (e, f) ϵ , (g, h) K , (i, j) L_0 , (k, l) L_B respectively. Here, China is divided into four subregions, north China (NC), northwest China (NWC), south China (SC) and southwest China (SWC), respectively.



Deleted:

Deleted: squared Brunt-Vaisälä frequency (

Deleted:)... below 3.0 km above ground level (AGL) for 2023 at (a) 00 UTC and (b) 12 UTC, (c, d) Richardson number (Ri)

Formatted: Not Highlight

Deleted:)... (e, f) turbulent dissipation rate (

Deleted:)... (g, h) vertical eddy diffusivity (

Deleted:)... (i, j) inner scale (

Formatted: Not Highlight

Deleted:)... (k, l) buoyancy length scale (

Formatted: Not Highlight

Deleted:)

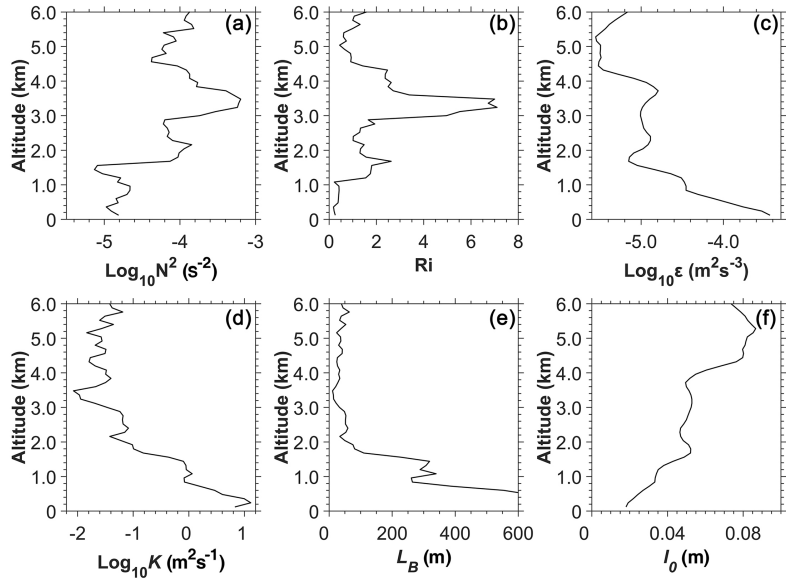
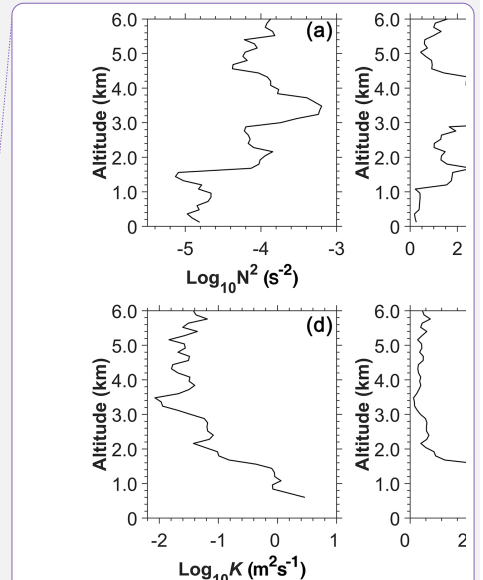


Figure 4. Vertical profiles of (a) N^2 , (b) Ri , (c) ϵ , (d) K , (e) L_B and (f) l_0 at 12 UTC for 16 July 2023 at Minfeng in northwest China. Note that N^2 is deduced from the sorted θ , it shows no regions of negative stability, however, Ri is inferred from the unsorted θ profile.



Deleted:

Deleted: squared Brunt Vaisalä frequency (

Deleted:)

Deleted: Richardson number (

Deleted:)

Formatted: Not Highlight

Deleted: turbulence dissipation rate (

Deleted:)

Deleted: vertical eddy diffusivity (

Deleted:)

Deleted: buoyancy length scale (

Formatted: Not Highlight

Deleted:)

Deleted: inner scale (

Deleted:)

Formatted: Not Highlight

Deleted: potential temperature (

Deleted:)

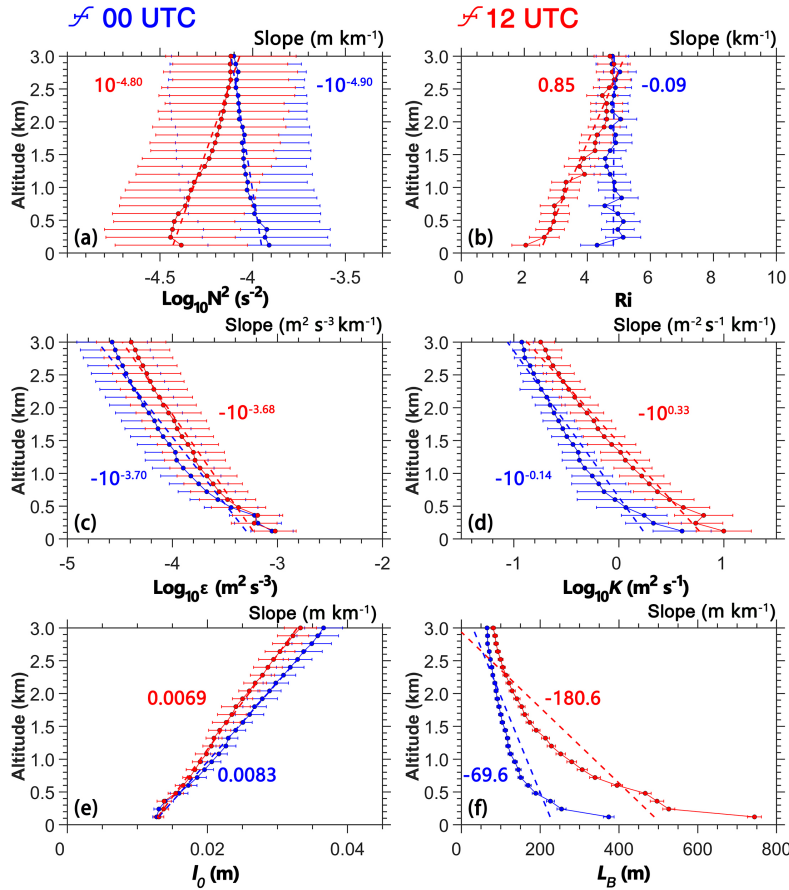


Figure 5. Vertical profiles of (a) N^2 , (b) Ri , (c) ϵ , (d) K , (e) l_0 and (f) L_B in the 0.12 to 3.0 km altitude range AGL at 00 UTC (blue) and 12 UTC (red) for 2023, and the slope values of turbulence-related parameters with altitude are also given in each panel where red and blue values represent 00 UTC and 12UTC, respectively.

Deleted: squared Brunt Vaisalä frequency (

Deleted: Richardson number (

Formatted: Not Highlight

Deleted:)

Deleted:)

Deleted: turbulent dissipation rate (

Deleted:)

Deleted: vertical eddy diffusivity (

Deleted:)

Deleted: inner scale (

Formatted: Not Highlight

Deleted:)

Deleted: buoyancy length scale (

Formatted: Not Highlight

Deleted:)

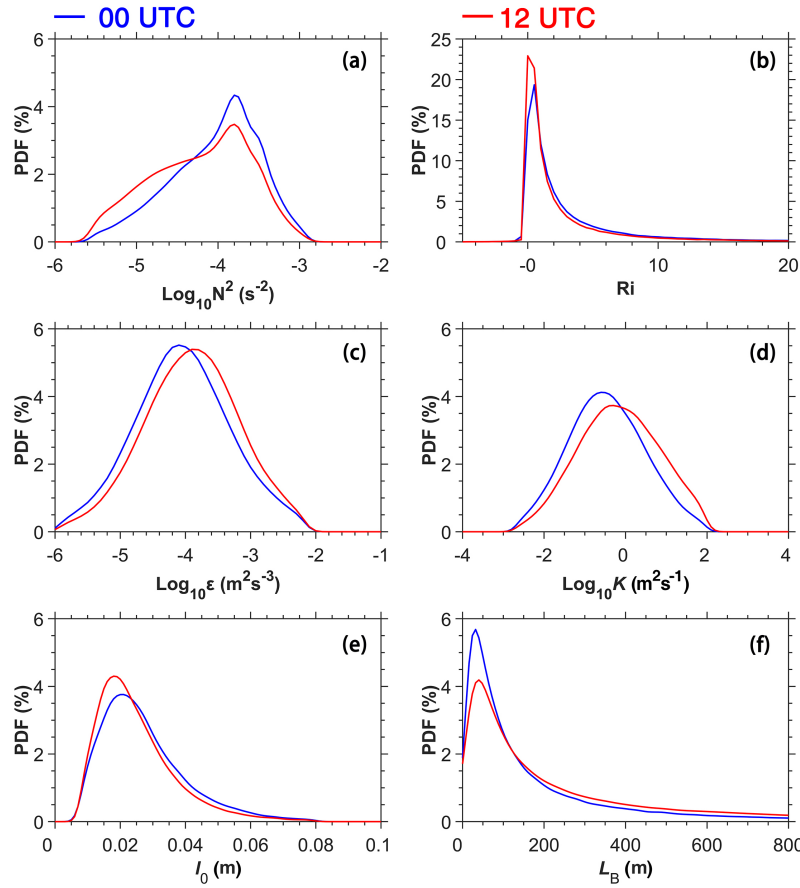


Figure 6. The probability density functions (PDF) of (a) N^2 , (b) Ri , (c) ϵ , (d) K , (e) l_0 and (f) L_B in the 0.12 to 3.0 km altitude range AGL at 00 UTC (blue) and 12 UTC (red) for 2023, respectively.

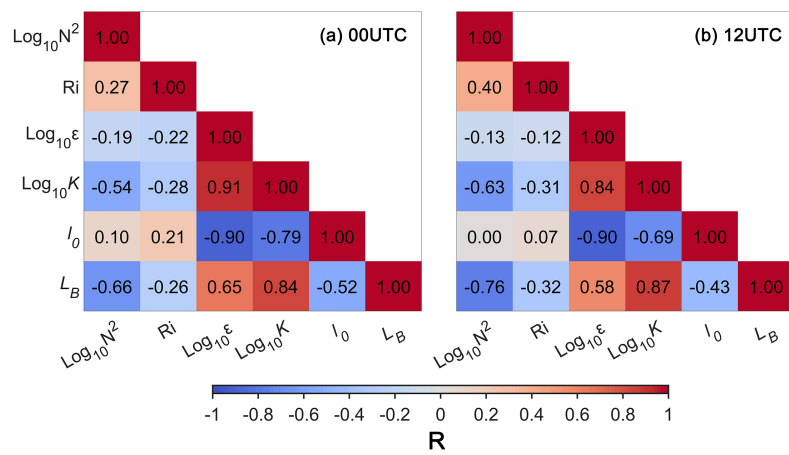


Figure 7. The correlation coefficients between turbulence-related parameters at (a) 00 UTC, (b) 12 UTC, respectively

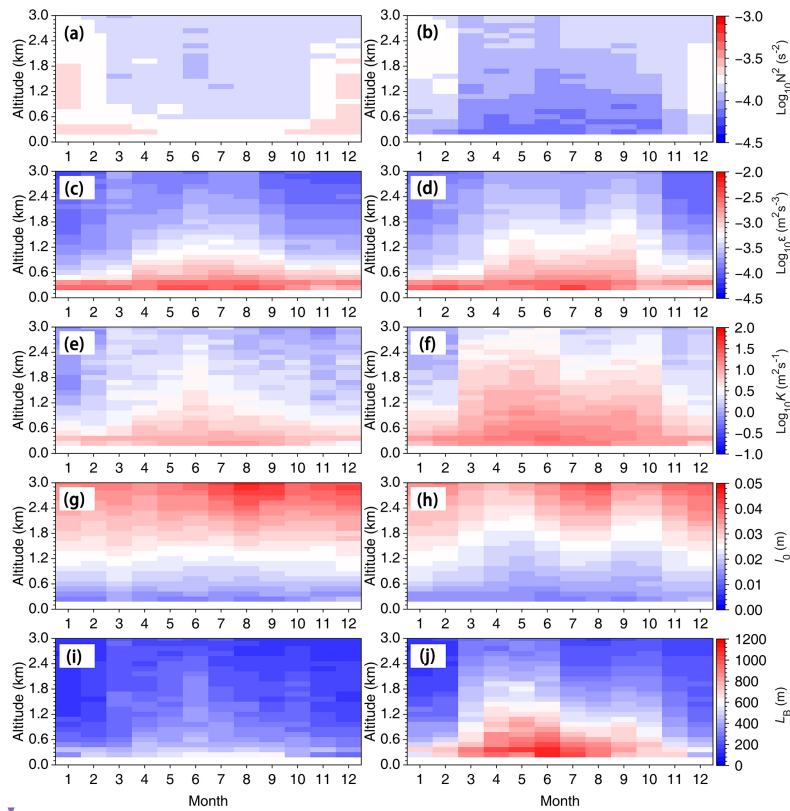
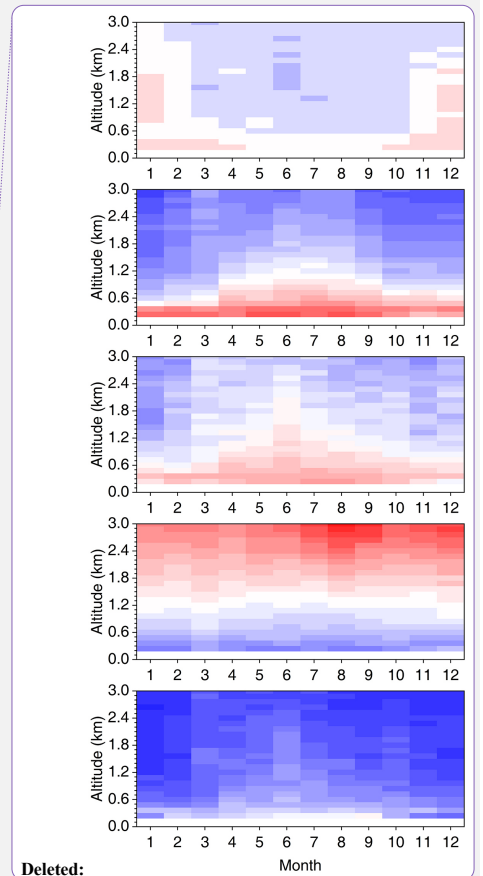


Figure 8. Monthly variation of (a) N^2 , (b) Ri , (c) ϵ , (d) K , (e) L_0 and (f) L_B in the 0.12 to 3.0 km altitude range AGL at 00 UTC (left) and 12 UTC (right) for 2023, respectively.



Deleted:

Deleted: squared Brunt Vaisalä frequency (

Deleted:)... (b) Richardson number (

[13]

Deleted:)... (c) turbulent dissipation rate (

[14]

Deleted:)... (d) vertical eddy diffusivity (

[15]

Formatted: Not Highlight

Deleted:)... (e) inner scale (

[16]

Formatted: Not Highlight

Deleted:)...and (f) buoyancy length scale (

[17]

Formatted: Not Highlight

Deleted:)

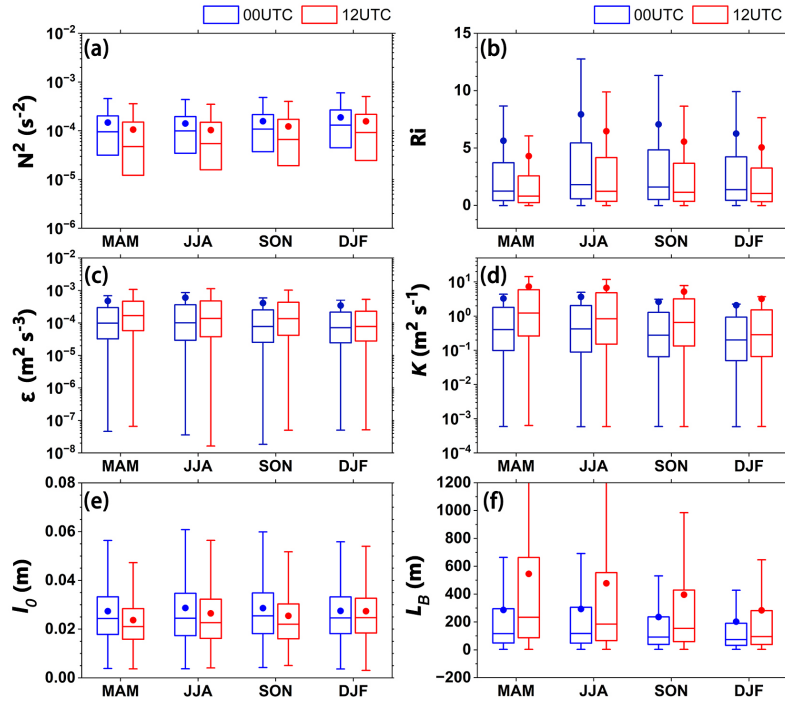


Figure 9. Box plot of seasonal (a) N^2 , (b) Ri , (c) ϵ , (d) K , (e) l_0 and (f) L_B in the 0.12-3.0 km altitude range at 00 UTC (light blue) and 12 UTC (light red) for 2023, respectively. Note that the median is shown as a line, the mean value is displayed as a circle, whereas the outer boundaries of the boxes represent the 25th and 75th percentiles, and the lines represent the interquartile range (IQR). Seasonal divisions are MAM (March-May), JJA (June-August), SON (September-November), DJF (December-February), respectively.

Deleted: squared Brunt Vaisalä frequency (

Deleted:)

Formatted: Not Highlight

Deleted: Richardson number (

Deleted:)

Deleted: turbulent dissipation rate (

Deleted: vertical eddy diffusivity (

Deleted:)

Deleted:)

Deleted: inner scale (

Formatted: Not Highlight

Deleted:)

Deleted: buoyancy length scale (

Formatted: Not Highlight

Deleted:)

Deleted: height

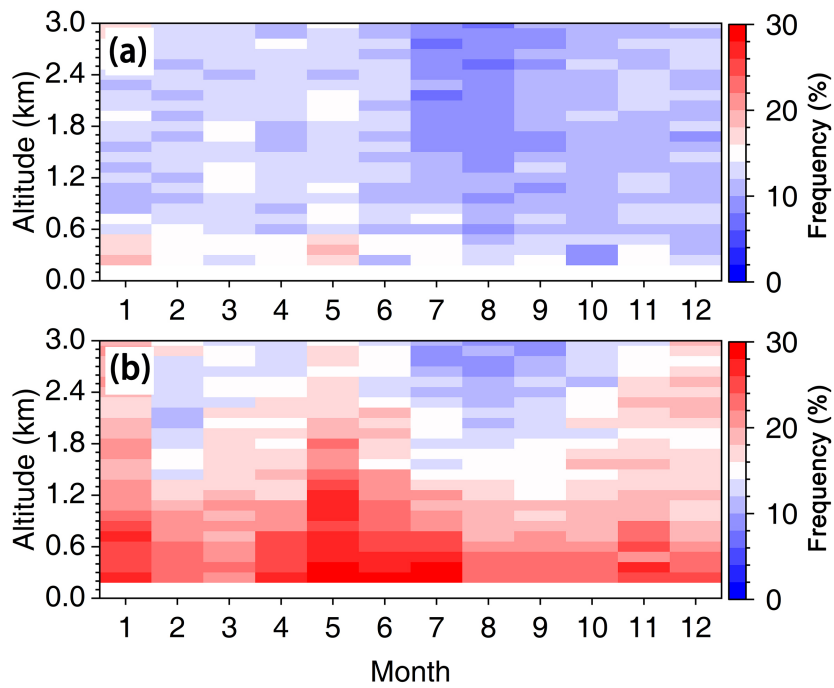


Figure 10. Monthly variation of occurrence frequency of $Ri < 0.25$ as a function of altitude, spanning from 0.12 to 3.0 km AGL at 00 UTC (a) and 12 UTC (b) for the year of 2023, respectively.

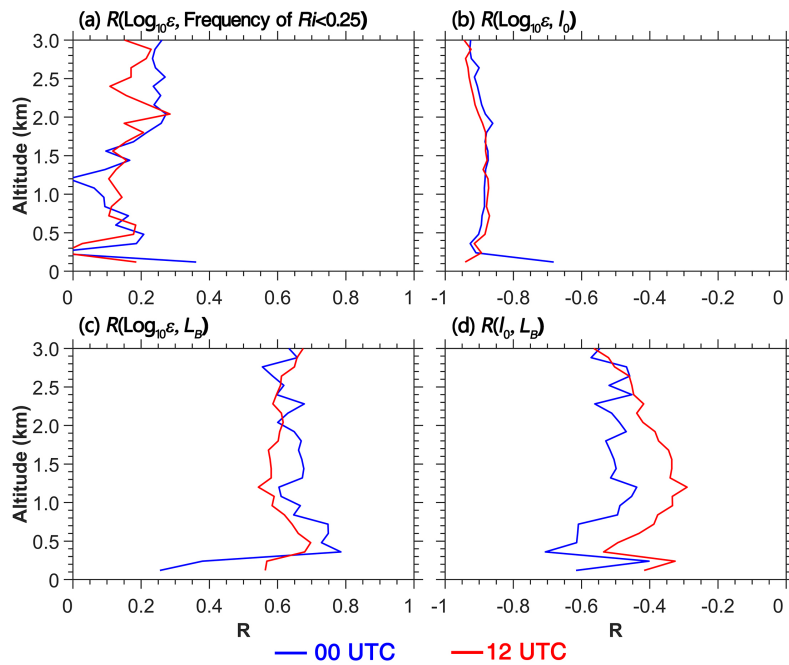


Figure 11. Profiles of correlation coefficient (R) between (a) $\text{Log}_{10}\varepsilon$ and the frequency of $Ri < 0.25$ at 00 UTC (blue) and 12 UTC (red). (b) Same as (a) but for the correlations of $\text{Log}_{10}\varepsilon$ with l_0 . (c) Same as (a) but for the correlation of $\text{Log}_{10}\varepsilon$ with L_B . (d) Correlations for l_0 and L_B in the inertial subrange, respectively.

Deleted: turbulent dissipation rate (

Deleted:)

Formatted: Not Highlight

Deleted: inner scale (

Deleted:)

Formatted: Not Highlight

Formatted: Not Highlight

Deleted:)

Deleted: buoyancy length scale (

Page 9: [1] Formatted JG 30/04/2025 17:19:00

Superscript, Not Highlight

Page 9: [1] Formatted JG 30/04/2025 17:19:00

Superscript, Not Highlight

Page 9: [1] Formatted JG 30/04/2025 17:19:00

Superscript, Not Highlight

Page 9: [1] Formatted JG 30/04/2025 17:19:00

Superscript, Not Highlight

Page 9: [2] Formatted JG 30/04/2025 17:19:00

Not Highlight

Page 9: [2] Formatted JG 30/04/2025 17:19:00

Not Highlight

Page 9: [3] Formatted JG 30/04/2025 17:19:00

Not Highlight

Page 9: [3] Formatted JG 30/04/2025 17:19:00

Not Highlight

Page 9: [4] Deleted mengdeli 28/04/2025 16:59:00

Page 9: [4] Deleted mengdeli 28/04/2025 16:59:00

Page 9: [5] Deleted mengdeli 28/04/2025 16:59:00

Page 9: [5] Deleted mengdeli 28/04/2025 16:59:00

Page 9: [6] Formatted JG 30/04/2025 17:19:00

Not Highlight

Page 9: [6] Formatted JG 30/04/2025 17:19:00

Not Highlight

Page 9: [7] Deleted mengdeli 28/04/2025 17:04:00

Page 9: [7] Deleted mengdeli 28/04/2025 17:04:00

Page 27: [8] Deleted mengdeli 28/04/2025 16:39:00



Page 27: [8] Deleted mengdeli 28/04/2025 16:39:00



Page 27: [9] Deleted mengdeli 28/04/2025 16:39:00



Page 27: [9] Deleted mengdeli 28/04/2025 16:39:00



Page 27: [10] Deleted mengdeli 28/04/2025 16:39:00



Page 27: [10] Deleted mengdeli 28/04/2025 16:39:00



Page 27: [11] Deleted mengdeli 28/04/2025 16:39:00



Page 27: [11] Deleted mengdeli 28/04/2025 16:39:00



Page 27: [12] Deleted mengdeli 28/04/2025 16:39:00



Page 27: [12] Deleted mengdeli 28/04/2025 16:39:00



Page 32: [13] Deleted mengdeli 28/04/2025 16:42:00



Page 32: [13] Deleted mengdeli 28/04/2025 16:42:00



Page 32: [14] Deleted mengdeli 28/04/2025 16:43:00



Page 32: [14] Deleted mengdeli 28/04/2025 16:43:00



Page 32: [15] Deleted mengdeli 28/04/2025 16:43:00



Page 32: [15] Deleted mengdeli 28/04/2025 16:43:00



▲
Page 32: [16] Deleted mengdeli 28/04/2025 16:43:00

▼

▲
Page 32: [16] Deleted mengdeli 28/04/2025 16:43:00

▼

▲
Page 32: [17] Deleted mengdeli 28/04/2025 16:43:00

▼

▲
Page 32: [17] Deleted mengdeli 28/04/2025 16:43:00

▼

▲